Observations of Titan's Stratosphere during Northern Summer: Temperatures, CH₃CN and CH₃D Abundances

Alexander E. Thelen[1,2] , Conor A. Nixon[2] , Martin A. Cordiner[2,3] , Emmanuel Lellouch[4] , Sandrine Vinatier[4] ,
Nicholas A. Teanby[5] , Bryan Butler[6] , Steven B. Charnley[2] , Richard G. Cosentino[7] , Katherine de Kleer[1] ,
Patrick G. J. Irwin[8] , Mark A. Gurwell[9] , Zbigniew Kisiel[10] , and Raphael Moreno[4]

[1] Division of Geological and Planetary Sciences, California Institute of Technology, Pasadena, CA 91125, USA; athelen@caltech.edu
[2] Solar System Exploration Division, NASA Goddard Space Flight Center, Greenbelt, MD 20771, USA
[3] Department of Physics, Catholic University of America, Washington, DC 20064, USA
[4] LESIA, Observatoire de Paris, Université PSL, Sorbonne Université, Université Paris Cité, CNRS, 92195 Meudon, France
[5] School of Earth Sciences, University of Bristol, Bristol, UK
[6] National Radio Astronomy Observatory, Socorro, NM 87801, USA
[7] Space Telescope Science Institute, Baltimore, MD 21218, USA
[8] Atmospheric, Oceanic and Planetary Physics, Clarendon Laboratory, Oxford OX1 3PU, UK
[9] Center for Astrophysics | Harvard & Smithsonian, Cambridge, MA 02138, USA
[10] Institute of Physics, Polish Academy of Sciences, Al. Lotników 32/46, 02-668 Warszawa, Poland

Abstract

Titan's atmospheric composition and dynamical state have previously been studied over numerous epochs by both ground- and space-based facilities. However, stratospheric measurements remain sparse during Titan's northern summer and fall. The lack of seasonal symmetry in observations of Titan's temperature field and chemical abundances raises questions about the nature of the middle atmosphere's meridional circulation and evolution over Titan's 29 yr seasonal cycle that can only be answered through long-term monitoring campaigns. Here, we present maps of Titan's stratospheric temperature, acetonitrile (or methyl cyanide; CH_3CN) abundance, and monodeuterated methane (CH_3D) abundance following Titan's northern summer solstice obtained with Band 9 ($\sim$0.43 mm) Atacama Large Millimeter/submillimeter Array observations. We find that increasing temperatures toward high southern latitudes, currently in winter, resemble those observed during Titan's northern winter by the Cassini mission. Acetonitrile abundances have changed significantly since previous (sub)millimeter observations, and we find that the species is now highly concentrated at high southern latitudes. The stratospheric CH_3D content is found to range between 4 and 8 ppm in these observations, and we infer the CH_4 abundance to vary between $\sim$0.9% and 1.6% through conversion with previously measured D/H values. A global value of $CH_4 = 1.15\%$ was retrieved, lending further evidence to the temporal and spatial variability of Titan's stratospheric methane when compared with previous measurements. Additional observations are required to determine the cause and magnitude of stratospheric enhancements in methane during these poorly understood seasons on Titan.

Unified Astronomy Thesaurus concepts: Titan (2186); Saturnian satellites (1427); Planetary atmospheres (1244); Planetary science (1255); Atmospheric composition (2120); Atmospheric variability (2119); Submillimeter astronomy (1647); Radio astronomy (1338); Radiative transfer (1335)

1. Introduction

Titan's atmosphere contains relatively high amounts of methane (CH_4) that, when dissociated along with molecular nitrogen (N_2), forms an expansive network of trace chemical species (see, for example, the reviews by Bézard et al. 2014; Hörst 2017; Nixon 2024). The distribution of these nitriles and organics both influences and is influenced by Titan's global circulation (Hourdin et al. 1995; Rannou et al. 2004; Newman et al. 2011; Lebonnois et al. 2014; Lora et al. 2015; Lombardo & Lora 2023), which changes with Titan's long ($\sim$7 yr) seasons during which longer-lived photochemical products accumulate at the shrouded winter pole (e.g., Teanby et al. 2008a, 2017). These chemical products also impact Titan's atmospheric energy budget through the absorption and radiation of infrared and UV photons (Yelle 1991; Tomasko et al. 2008; Bézard et al. 2018). Thus, the temporal and spatial distribution of Titan's trace species and the

effects of their radiative exchange with the atmosphere require investigation of the middle atmosphere (stratosphere and mesosphere; $\sim$100−500 km) throughout Titan's 29.5 yr orbit. Great strides in this formidable task have been enabled by the Cassini/Huygens mission and the multitude of measurements presented in recent years on the detection of trace molecules and isotopic ratios (Bézard et al. 2007; Vinatier et al. 2007; Coustenis et al. 2008; Nixon et al. 2008, 2012, 2013; Jennings et al. 2008, 2009; Jolly et al. 2010, 2015) and seasonal variability in temperature, winds, and composition (Coustenis et al. 2007, 2010, 2016, 2018, 2020; Vinatier et al. 2007, 2010, 2015, 2020; Teanby et al. 2008b, 2008a, 2010a, 2012, 2017, 2019; Achterberg et al. 2008, 2011; Cottini et al. 2012; Sylvestre et al. 2018; Sharkey et al. 2020; Mathé et al. 2020; Sharkey et al. 2021; Achterberg 2023). These studies form the foundation for continued monitoring of Titan's atmospheric state during portions of Titan's year beyond the Cassini mission (2004–2017; $L_S \sim 300°−90°$), provoking questions and an impetus for further investigations of novel chemical pathways, exogenic energy sources and processes, and the origin and resupply of its crucial methane reservoir (Tobie et al. 2006; Lunine & Atreya 2008;

Lellouch et al. 2014; Glein 2015; Davies et al. 2016; Nixon et al. 2018; Miller et al. 2019).

Following the end of the Cassini mission near Titan's northern summer solstice, ground-based investigations may provide insights into changes occurring in the stratosphere and lower mesosphere as influenced by the heretofore unmonitored seasonal changes. Chemical species with both relatively short (<1 yr) and long (e.g., tens to hundreds of yr) photochemical lifetimes can be used as a probe of global-scale atmospheric dynamics driven by Titan's pole-to-pole circulation cell (and, near the equinoxes, two equator-to-pole cells). Species such as hydrogen cyanide (HCN) and CH_3CN, with stratospheric lifetimes of tens of yr (Yung et al. 1984; Wilson & Atreya 2004; Krasnopolsky 2009, 2014; Dobrijevic et al. 2014; Loison et al. 2015; Willacy et al. 2016; Vuitton et al. 2019), show distributions with lingering enhancements over Titan's winter pole until the spring. This is largely due to the accumulation of trace species from the subsiding branch of the global circulation cell during winter, which are then confined within the boundary of the circumpolar vortex at latitudes >60° and persist due to relatively slow or inefficient photochemical destruction (Coustenis et al. 2010; Teanby et al. 2008b, 2009a, 2009b, 2010b; Vinatier et al. 2015, 2020; Mathé et al. 2020; Sharkey et al. 2020, 2021; Achterberg 2023). These distributions can be contrasted with gases of short photochemical lifetimes (e.g., cyanoacetylene, HC_3N), which exhibit rapid enhancements over the fall pole shortly after equinox and are depleted at other latitudes (Thelen et al. 2019b; Teanby et al. 2019; Vinatier et al. 2015, 2020; Cordiner et al. 2019).

Additionally, there exists the curious case of Titan's stratospheric methane, which is thought to be uniformly mixed over seasonal timescales (Wilson & Atreya 2004; Niemann et al. 2005) but has been shown to potentially be modified by convective injection from localized regions in the troposphere (Lellouch et al. 2014). Though Titan's methane distribution was thought to be relatively constant above the troposphere and may not show substantial variability with latitude, altitude, and time (often defined using the Huygens measurements presented in Niemann et al. 2010), Lellouch et al. (2014) inferred that the CH_4 mixing ratio varied from ~1% to 1.5% between Titan's tropical (~0°–20°) and temperate (~30°–40°) latitudes through measurements with the Cassini Composite Infrared Spectrometer (CIRS) instrument. Subsequent analysis of four Cassini occultations with the Visual Infrared Mapping Spectrometer (VIMS), initially by Maltagliati et al. (2015) and reanalyzed in Rannou et al. (2021, 2022), resulted in stratospheric methane measurements closer to ~1.1%, with localized vertical and latitudinal enhancements. A reanalysis of spectra recorded by the Descent Imager and Spectral Radiometer (DISR) instrument during the descent of the Huygens probe also suggests that the CH_4 mixing ratio decreases with altitude in Titan's stratosphere, reaching a value of ~1% at altitudes above 110 km (Rey et al. 2018). Together, the measurements of CH_4 and various trace gases allow for the inference of global, and potentially local, circulation and meteorological events that affect the composition and dynamics of the stratosphere, which in turn affect the energy budget of the upper atmosphere and precipitation from the troposphere onto the surface (Yelle 1991; Hourdin et al. 1995; Rannou et al. 2004, 2006; Crespin et al. 2008; Tomasko et al. 2008; Mitchell et al. 2009; Mitchell 2012; Lebonnois et al. 2012, 2014; Lora et al. 2015; Lombardo & Lora 2023).

In recent years, far-IR and (sub)millimeter observations from facilities such as the Institut de Radioastronomie Millimétrique 30 m telescope and interferometer, the Submillimeter Array, the Atacama Large Millimeter/submillimeter Array (ALMA), and the Herschel Space Telescope have provided the means by which to complement and continue the investigation of Titan's substantial, complex atmosphere. Early ground- and space-based (sub)millimeter observations of Titan allowed for the confirmation of H_2O and HC_3N following their detections with the Infrared Space Observatory (ISO; Coustenis et al. 1998) and Voyager 1 spacecraft (Kunde et al. 1981), the first detections of HNC and acetonitrile (or methyl cyanide; CH_3CN), and the derivation of vertical abundance and temperature profiles (Bézard et al. 1992, 1993; Marten et al. 2002; Gurwell 2004; Courtin et al. 2011; Rengel et al. 2011, 2014, 2022; Moreno et al. 2011, 2012a; Bauduin et al. 2018). Highly resolved spectroscopic measurements provided the means by which to derive Titan's wind speeds between the upper stratosphere and the thermosphere through Doppler shifts (Moreno et al. 2005; Lellouch et al. 2019; Cordiner et al. 2020; Light et al. 2024). Through the measurement of rotational transitions of thermal tracers such as carbon monoxide (CO) and HCN, ALMA has recently allowed for the derivation of Titan's vertical temperature profiles throughout the stratosphere and mesosphere and into the lower thermosphere (Serigano et al. 2016; Thelen et al. 2018; Lellouch et al. 2019; Thelen et al. 2022). Additionally, its high spectral resolution and extensive frequency coverage enable resolved emission line profiles of many organic molecules—some of which were unable to be detected by Cassini in the infrared, including C_2H_5CN, C_2H_3CN, and others (Cordiner et al. 2015; Palmer et al. 2017; Cordiner et al. 2019; Thelen et al. 2019b, 2020; Nixon et al. 2020). Finally, ALMA has provided the means by which to monitor Titan's atmospheric CH_4 content in the stratosphere by way of monodeuterated methane (CH_3D; Thelen et al. 2019a), which has previously been measured in the IR through ground- and space-based facilities and used to derive Titan's deuterium-to-hydrogen ratio (D/H). Early measurements from Voyager and ground-based IR observatories are discussed in Penteado et al. (2005, and references therein), while the values derived from Cassini data are detailed in Nixon et al. (2012). The distribution and modification of these molecular abundance profiles can provide global snapshots of the dynamical state of the atmosphere, while the derived temperature profiles and winds measured from Doppler shifts helps to complete the picture of the seasonal evolution of Titan's atmosphere (Hörst 2017; Nixon et al. 2018; Teanby et al. 2019).

Here, we present the analysis of ALMA data acquired in 2022 June ($L_S \approx 146°$, during the transition of Titan's northern hemisphere from summer into fall), designed to investigate both the long-term evolution of Titan's temperature and chemical abundances. In particular, the measurement of rotational CH_3D transitions allows for a comparison to recent Cassini studies showing a CH_4 distribution influenced by complex tropospheric and stratospheric interplay; further, ALMA allows for the vertical and spatial distribution of CH_3CN to be investigated for the first time, providing an additional tracer of seasonal dynamics (Thelen et al. 2019b). The results of CH_3CN mapping can be compared to HCN and other long-lived chemicals that were measured by Cassini (e.g., CO_2, C_2H_6) throughout Titan's year. These measurements,

Table 1
Observed Spectral Transitions

Species	Transition[a]	Rest Freq. (GHz)	E_u (K)
CO	$6 \rightarrow 5$	691.473	116.16
CH$_3$D	$3_2 \rightarrow 2_2$	697.691	74.86
	$3_1 \rightarrow 2_1$	697.759	68.95
	$3_0 \rightarrow 2_0$	697.781	66.98
CH$_3$CN	$38_9 \rightarrow 37_9$	697.209	1230.80
	$38_8 \rightarrow 37_8$	697.434	1109.86
	$38_7 \rightarrow 37_7$	697.632	1003.08
	$38_6 \rightarrow 37_6$	697.804	910.50
	$38_5 \rightarrow 37_5$	697.949	832.12
	$38_4 \rightarrow 37_4$	698.068	767.97
	$38_3 \rightarrow 37_3$	698.161	718.06
	$38_2 \rightarrow 37_2$	698.227	682.40
	$38_1 \rightarrow 37_1$	698.267	661.00
	$38_0 \rightarrow 37_0$	698.281	653.86

Note. Spectral line positions and upper level energies (E_u) are taken from the CDMS: https://cdms.astro.uni-koeln.de/classic/entries/ (Müller et al. 2001, 2005; Endres et al. 2016).
[a] Rotational transitions are denoted as $Ju \rightarrow Jl$ or $Ju_{Kl} \rightarrow Jl_{Kl}$, where u and l represent the upper and lower energy states, respectively, and K represents the angular momentum quantum number.

along with Titan's temperature field, are investigated here during a period with very limited prior observational coverage. The observational details are described in Section 2, followed by the description of the radiative transfer modeling employed to derive temperature and abundance information in Section 3. The resulting atmospheric retrievals and the discussion, comparisons to prior measurements, and implications are presented in Section 4. A summary of our conclusions is provided in Section 5.

2. Observations

The primary array of the ALMA facility is comprised of 50 12 m antennas located on the Chajnantor plateau in the Atacama Desert, Chile. Titan was observed by 44–48 antennas on 2022 June 18 and 29 in ALMA Band 9 (602−720 GHz; ~0.4−0.5 mm), simultaneously targeting the rotational transitions of CO ($J = 6$–5), HCN ($J = 8$–7), CH$_3$CN ($J = 38$–37), and the CH$_3$D $J = 3$–2 triplet located between 690 and 710 GHz for ALMA Project #2021.1.01388.S. The observed rotational transitions are detailed in Table 1. The targeted spectral windows were set to resolutions of 488 kHz (HCN), 977 kHz (CH$_3$CN, CH$_3$D), and 1129 kHz (CO, continuum window). Millimeter observations at high frequencies are significantly impacted by the Earth's atmosphere directly above the facility through the reduced atmospheric transmittance and the precipitable water vapor content, which produces interferometric phase artifacts that reduce the image coherence (analogous to optical "seeing" effects). As such, the high-frequency transitions of many known trace chemical species have yet to be observed on Titan (or beyond) through interferometry. While Serigano et al. (2016) and Thelen et al. (2019b) observed high-frequency transitions of CO ($J = 6$–5), HCN ($J = 8$–7), and CH$_3$CN ($J = 37$–36), the $J = 3$–2 rotational CH$_3$D transitions have yet to be definitively observed in astrophysical environments (though the $J = 2$–1 transitions were previously detected on Titan; see Thelen et al. 2019a).

Fortunately, the relatively low (~0.3–0.5 mm) precipitable water vapor measurements during the observation dates resulted in low phase scatter, which facilitates observations with the moderately extended ALMA array, which was set to configuration C-5 with maximum antenna separations of up to ~1.4 km. While the ALMA data were reduced with the standard pipeline procedures provided by the Joint ALMA Observatory in the Common Astronomy Software Applications (CASA; Jaeger 2008) ver. 6.2, additional iterative self-calibration and imaging procedures were performed so as to improve the image coherence and signal-to-noise ratio (S/N), executed similarly to those used for the Galilean satellites and giant planets (de Pater et al. 2019; de Kleer et al. 2021; Camarca et al. 2023; Thelen et al. 2024). First, the CH$_3$CN spectral window and a relatively featureless spectral window from the correlator upper sideband at ~712 GHz were used to create a single continuum image of Titan by combining data from both ALMA executions. We flagged out all strong spectral line channels from atmospheric trace species and then concatenated the remaining averaged continuum channels using the multifrequency synthesis settings in the CASA `tclean` algorithm. Using a starting model of a flat or limb-darkened disk at the appropriate brightness temperature of Titan's Band 9 continuum, we solved for phase solutions as a function of time on this continuum image with successively smaller solution intervals until phase scatter due to noisy antenna baselines was sufficiently minimized; see the reviews in Cornwell & Fomalont (1999), Butler & Bastian (1999), Brogan et al. (2018), and ALMA Memo #620 (Richards et al. 2022) for further details on the self-calibration of bright, compact sources such as planetary disks. Once the continuum phase distribution was on order ±10%, we applied these phase solutions to the full calibrated spectral line data and performed further image deconvolution on the combined executions to obtain the final spectral image cube. This round of imaging was performed using the CASA `tclean` task with the Högbom algorithm, natural antenna weighting, and 0″01 square pixels, resulting in a final angular resolution (represented by the ALMA beam) of 0″172 × 0″148 (~1000 km on Titan at the time of observation) with a position angle of 71°.49. Compared to Titan's angular size of ~1″0 (including its 2575 km solid-body radius and atmosphere up to 1200 km) during the time of observation, this resolution allowed us to observe localized emission from a number of distinct latitude regions ranging from ~77°S to 90°N.

A latitudinally averaged spectrum extracted from ~150 km above Titan's solid surface, where the CH$_3$D emission is strong, is presented in Figure 1, showing the stronger CH$_3$CN $J = 38$–37 transitions surrounding the broad CH$_3$D $J = 3$–2 triplet. Emission maps produced by the integration of channels across this spectral range at every pixel are shown in Figure 2 for the CH$_3$D and CH$_3$CN rotational bands, as well as an image of the continuum emission for reference. While the emission from CH$_3$CN is localized at high southern latitudes, the CH$_3$D emission map possesses a significantly lower S/N, preventing substantial conclusions regarding variations in the CH$_3$D distribution to be drawn from imaging alone. As in previous studies using ALMA to observe Titan, we extracted spectra at spatially independent regions to determine the variability of vertical profiles with latitude (see Figure 2(C)). The spatial resolution of these observations enabled the analysis of spectra from approximately 20° latitude bins, which were averaged
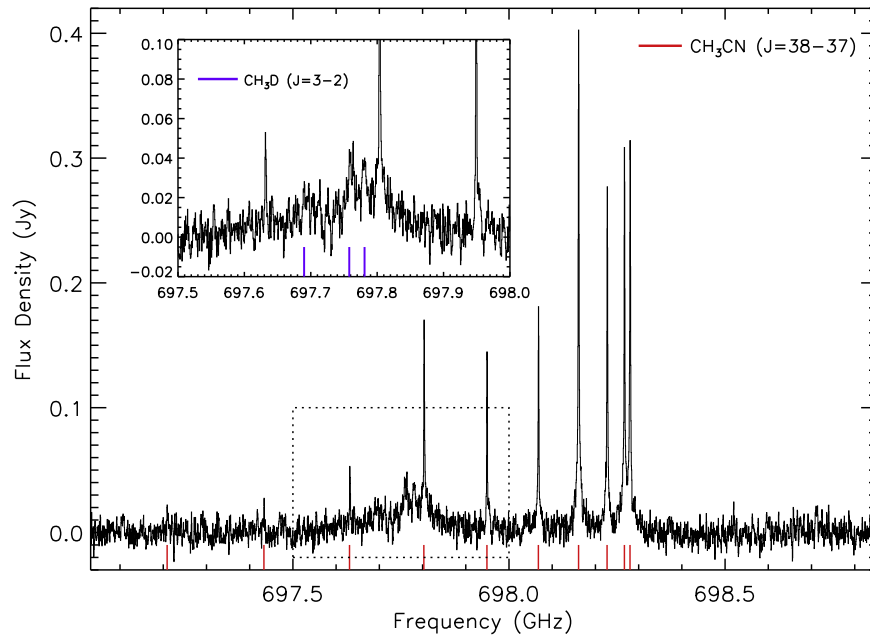
Figure 1. Limb-averaged Titan spectrum, created by averaging nine separate 20° latitude bins from both the eastern and western hemispheres following the combination of both ALMA executions during 2022 June. The spectral resolution was 977 kHz. Spectra were extracted from ∼150 km above the surface. Data are shown following continuum subtraction. Transitions of the CH_3CN ($J = 38–37$) band from the CDMS catalog, Doppler-shifted to Titan's rest velocity, are shown in red for reference; the line marker amplitudes are arbitrary. The dotted box denotes the spectral range of the figure inset, which focuses on the CH_3D ($J = 3–2$) triplet. The CH_3D transitions from the CDMS catalog are again denoted in vertical purple lines in the inset. As a result of the continuum subtraction, the extent of the pressure-broadened CH_3D band is evident, in comparison to the relatively narrow CH_3CN emission lines.

with the surrounding 5×5 pixel grid such as to improve the spectral S/N.

3. Radiative Transfer Modeling

Latitudinally averaged spectra were extracted from the regions denoted in Figure 2(C) (yellow squares) for use with the radiative transfer package Non-linear optimal Estimator for MultivariatE spectral analySIS (NEMESIS; Irwin et al. 2008; NEMESIS is publicly available online[11]). Wavenumber offsets on order 1×10^{-5} cm^{-1} were added to spectra where necessary to account for minor Doppler shifts due to Titan's wind field (Lellouch et al. 2019; Cordiner et al. 2020); this is about one-third of the ALMA channel spacing. Thirty line-of-sight emission angles were calculated for each individual spectrum extraction location so as to correctly model the emission originating from the corresponding ALMA beam footprint distributed around Titan's limb (Figure 2(C), yellow ellipses); see Thelen et al. (2018) for additional details on the construction of emission angles to represent the ALMA beam shape.

Spectral line frequencies, broadening and temperature-dependence parameters, and partition function coefficients were taken from the Cologne Database for Molecular Spectroscopy (CDMS) and the HITRAN database[12] (Rothman et al. 2005, 2013; Gordon et al. 2017, 2022) where available. The N_2-broadening parameters for CH_3CN were taken from Dudaryonok et al. (2015), as discussed in Thelen et al. (2019b). Collisionally induced absorption of N_2, CH_4, and H_2 pairs was parameterized as in previous studies of Titan with ALMA and Cassini/CIRS (Borysow & Frommhold 1986a, 1986b, 1986c, 1987; Borysow 1991; Borysow & Tang 1993).

Vertical profiles of these gases were used from the Huygens Gas Chromatograph Mass Spectrometer (GCMS) measurements (Niemann et al. 2005, 2010).

Following spectral extraction and conversion, NEMESIS forward models were generated for spectral regions containing only continuum emission (formed from the above absorption pairs and thermal radiation) to determine constant, multiplicative scaling factors to apply to the spectra due to flux calibration uncertainties; ALMA flux calibration uncertainties at high frequencies can be as high as 20% (See the ALMA Cycle 8-2021 Proposers Guide; Braatz et al. 2021). These models were initialized using the stratospheric temperature profile retrieved from recent, unresolved ALMA observations of Titan in 2019 (Thelen et al. 2020), along with tropospheric temperature profiles (which are not expected to show significant seasonal variability) from Cassini Radio Science measurements (Schinder et al. 2020) interpolated to the corresponding latitude regions. The spectral scaling factors were found to be between 0.85 and 1.15 for each spectral window.

The temperature profiles between the stratosphere and mesosphere were then retrieved using the CO ($J = 6–5$) emission line. Retrievals at each latitude bin were performed by allowing the disk-averaged temperature profile from Thelen et al. (2020) to continuously vary with altitude above ∼100 km while keeping the tropospheric temperatures from Schinder et al. (2020) and a nominal CO abundance of ∼50 parts per million (ppm; 1×10^{-6}), as determined by a number of studies (e.g., de Kok et al. 2007; Teanby et al. 2010b; Gurwell et al. 2011; de Bergh et al. 2012; Rengel et al. 2014; Serigano et al. 2016), held constant. Atmospheric temperatures were varied iteratively with the NEMESIS retrieval algorithm (based on the Levenberg–Marquardt principle; see, e.g., Press et al. 1992) to minimize differences between the data and model spectra (determined by the "cost function") and subsequently produced
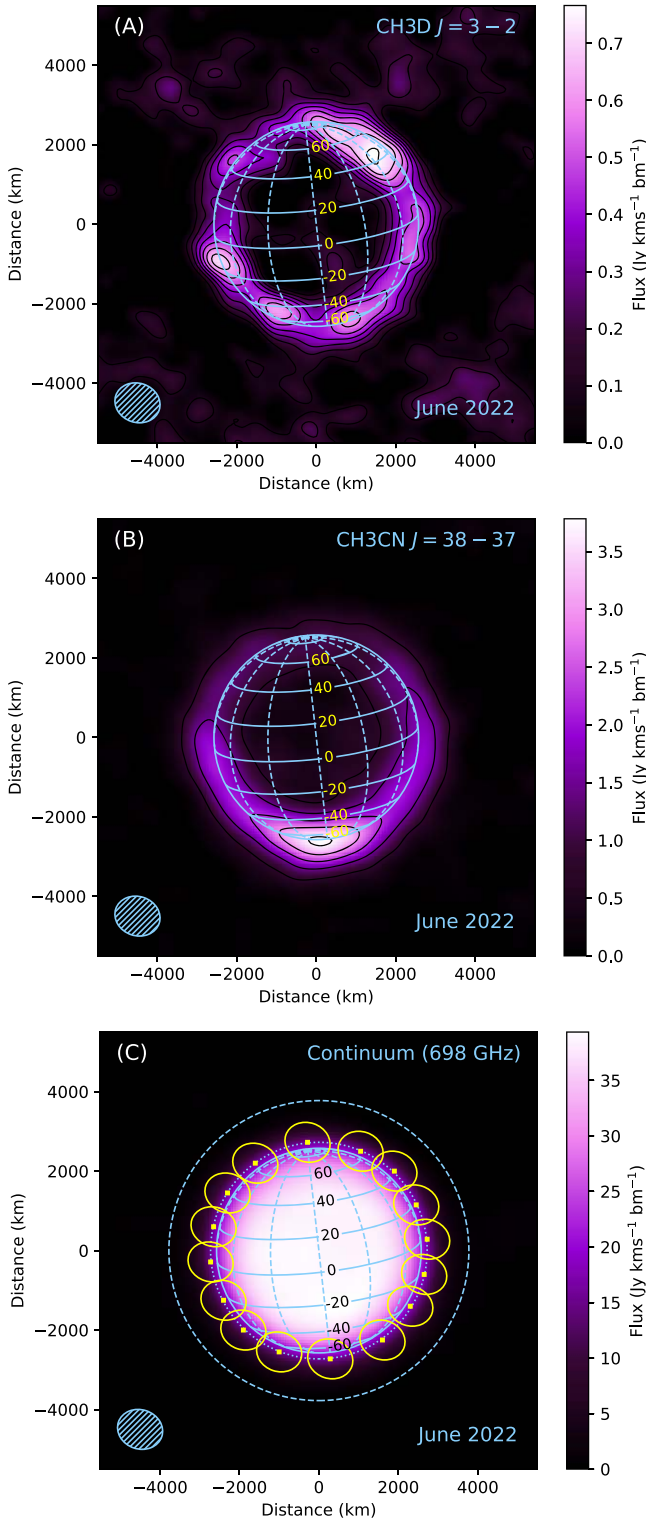
---

[11] https://nemesiscode.github.io
[12] https://hitran.org

Figure 2. Integrated emission (or "moment zero") maps of Titan's CH$_3$D (A), CH$_3$CN (B), and continuum (C) spectra. Panels (A) and (B) correspond to the emission integrated over the spectral transitions shown in Figure 1. The synthesized ALMA beam size (FWHM of the ALMA point-spread function) is shown as the hatched ellipse in the lower left; Titan's solid surface, latitude, and longitudes are shown (solid and dashed blue lines). Contours are in increments of 1σ (A) and 10σ (B). Spectra were extracted for radiative transfer modeling at 20° latitude bins as displayed on the continuum emission map in panel (C) (yellow squares), and the corresponding area representing the ALMA beam footprint used to generate synthetic spectra from these individual regions on Titan's limb is shown (yellow ellipses). Altitudes of 150 km and 1200 km above Titan's surface are denoted by dotted and dashed blue circles, respectively, on the continuum map.

parameters that reached a global, reduced χ^2 minimum (Irwin et al. 2008). The correlation length was taken to be 1.5 scale heights, and though the profiles were allowed to vary up to 1200 km, variations in the temperature profile above $\sim$600 km (1×10^{-3} mbar) did not contribute significantly to minimizing the reduced χ^2. The resulting temperature profiles were then used to retrieve the vertical CH$_3$CN abundance profile at each latitude starting with a combination of abundance profiles from observations by Marten et al. (2002) and photochemical predictions by Loison et al. (2015) above $\sim$400 km, as was done with previous ALMA observations (Thelen et al. 2019b). The five strongest spectral transitions of the CH$_3$CN ($J = 38-37$) band were used to retrieve the vertical profile without interference from the nearby CH$_3$D ($J = 3-2$) triplet (see Figure 1).

Finally, the aforementioned temperature and CH$_3$CN profiles were fixed for CH$_3$D retrievals. The a priori CH$_3$D profile was generated from the constant stratospheric measurement of CH$_4$ = 1.48% from the Huygens/GCMS (Niemann et al. 2010) and the D/H from the weighted average of measurements from ALMA and Cassini/CIRS of 1.2×10^{-4} (see Thelen et al. 2019a; Nixon et al. 2012, and references therein). As the individual CH$_3$D spectra had relatively low signal-to-noise, we performed retrievals on spectra from the eastern and western hemispheres simultaneously to better constrain the CH$_3$D abundance. These models were parameterized as a simple scaling of the input profile, as opposed to the continuous retrievals with altitude that were employed for higher-S/N spectral lines. Nearby CH$_3$CN lines were included in the model and were fit well by the input profiles from the previous retrievals. Representative ALMA data for CO, CH$_3$CN, and CH$_3$D are shown in Figure 3 compared to the best-fit NEMESIS models. Residual spectra show that the spectral lines are fit well using the methods described above.

4. Results and Discussion

4.1. Temperature Profiles

The resulting temperature profiles and corresponding errors retrieved from NEMESIS models of the CO ($J = 6-5$) transition are shown in Figures 4(A) and (B), respectively, throughout the stratosphere and mesosphere ($\sim$100$-$500 km; $\sim$10-1×10^{-3} mbar), where the spectral radiance is sensitive to changes in atmospheric temperature. The retrieved temperature profiles show a distinct difference in regions north and south of the equator, particularly at higher latitudes. Below the stratopause (often near $\sim$300 km or 0.1 mbar), temperatures from the northern hemisphere (warm colored profiles in Figure 4(A)) are elevated compared to those measured at both the equator (black profile) and southern hemisphere (cool colored profiles) by $\sim$10–20 K, particularly between 1 and 10 mbar ($\sim$100–200 km). Profiles retrieved at 40°S and 60°S are cooler than the equator by $\sim$7–10 K. Titan's radiative response timescale in the stratosphere is short enough that the atmosphere will respond (i.e., equilibrate) to the increased insolation in the northern hemisphere over $\sim$1 Earth yr, well within a Titan season (Flasar et al. 1981). Thus, the dichotomy between temperature profiles in the northern and southern hemispheres follows naturally from Titan's transition into its northern summer in 2017. While the radiative response time is lower in the mesosphere—so the altitudes above 300 km respond rapidly to insolation—the upper layer of Titan's pole-to-pole circulation cell also affects these
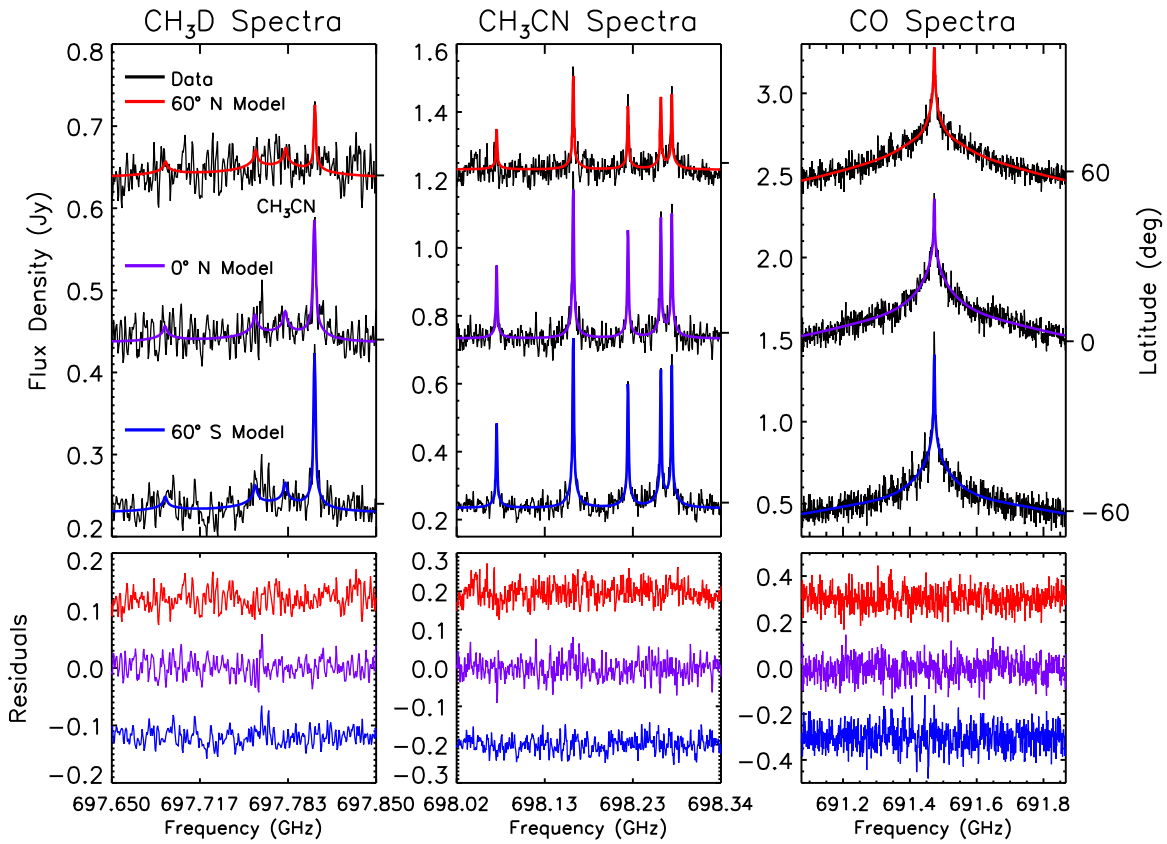
Figure 3. Top row: representative ALMA data (black) compared to synthetic spectra from the corresponding best-fit NEMESIS models at 60°N (red), the equator (purple), and 60°S (blue) for spectral ranges covering the CH_3D (left column), CH_3CN (middle column), and CO (right column) transitions. Spectra are offset by arbitrary, constant factors for clarity (0.2 Jy for CH_3D; 0.5 Jy for CH_3CN and CO). The interloping CH_3CN ($J = 38_6-37_6$) transition at 697.804 GHz is denoted in the equatorial CH_3D spectrum. Bottom row: residual (data–model) spectra corresponding to the data and models in the top row. Residual spectra are offset for clarity (0.12 Jy for CH_3D; 0.2 for CH_3CN; 0.3 for CO).

temperatures (see, e.g., Teanby et al. 2008a; Achterberg et al. 2011; Teanby et al. 2012; Vinatier et al. 2015). We find that profiles above 300 km (~0.1 mbar) are largely similar ±40° of the equator, but those at high latitudes show the influence of the meridional circulation. Northern hemispheric profiles at high latitudes are cooler than those at lower latitudes above the stratopause, likely due to air rising from below and cooling through adiabatic expansion. The subsiding branch of the circulation cell increases temperatures at the high southern latitudes, and, in particular, the highest southern latitudinal profile we can observe here (>77°S) exhibits the highest and warmest stratopause at 190 K between 320 and 350 km (purple profile in Figure 4(A)). While the profiles at low southern and northern latitudes are close together in magnitude, the stratopause may be slightly elevated (~20 km) at the highest southern latitudes (blue and purple lines in Figure 4(A)) compared to the profiles at the highest northern latitudes (orange and red lines). The measurement of temperature profiles in the mesosphere and thermosphere can be achieved using ALMA through the combination of CO and HCN emission lines (Lellouch et al. 2019; Thelen et al. 2022), which we leave to future work for these latitudes.

We derive vertical temperature profiles that are similar to those measured throughout the Cassini mission with the CIRS instrument (Achterberg et al. 2008; Teanby et al. 2010a; Achterberg et al. 2011; Vinatier et al. 2015; Coustenis et al. 2018; Teanby et al. 2019; Coustenis et al. 2020; Vinatier et al. 2020; Mathé et al. 2020), with lower stratospheric (<200 km; >1

mbar) temperatures ranging from ~130 to 170 K and increasing to a stratopause temperature of ~180–200 K. We observe the continuation of the trend observed through limb and nadir sounding of the atmosphere by CIRS toward the end of the Cassini mission in an elevated, warmer southern stratopause, which mirrors the initial measurements of Titan's northern polar temperatures during its northern winter at the start of the Cassini mission. This evolution is even apparent through the comparison of the profiles presented here and ALMA observations from 2015 (Figures 4(C) and (D)), which shows the increase in stratospheric temperatures below ~200 km in the north (Figure 4(C)), the cooling of the stratosphere at these altitudes in the south, and the possibility of a slightly elevated and warmer southern stratopause (Figure 4(D)). It should be noted that the vertical and angular resolution of the temperature profiles derived through these remote-sensing observations is not sufficient to capture potentially stark latitudinal differences toward the poles as observed in other works (e.g., those from the Cassini limb sounding observations; see, for example, Achterberg et al. 2008; Vinatier et al. 2015); as such, the magnitude of the stratopause altitude and temperature variability toward the poles may be somewhat diminished in these ALMA measurements. This is largely due to the ALMA beam size, which smoothed out the observed atmospheric state over ~10°–20° latitude (~2–5× that of many CIRS observations) and did not allow for the high degree of altitude sampling as achieved with Cassini/CIRS limb observations (Kunde et al. 1996; Flasar et al. 2004; Nixon et al. 2019).
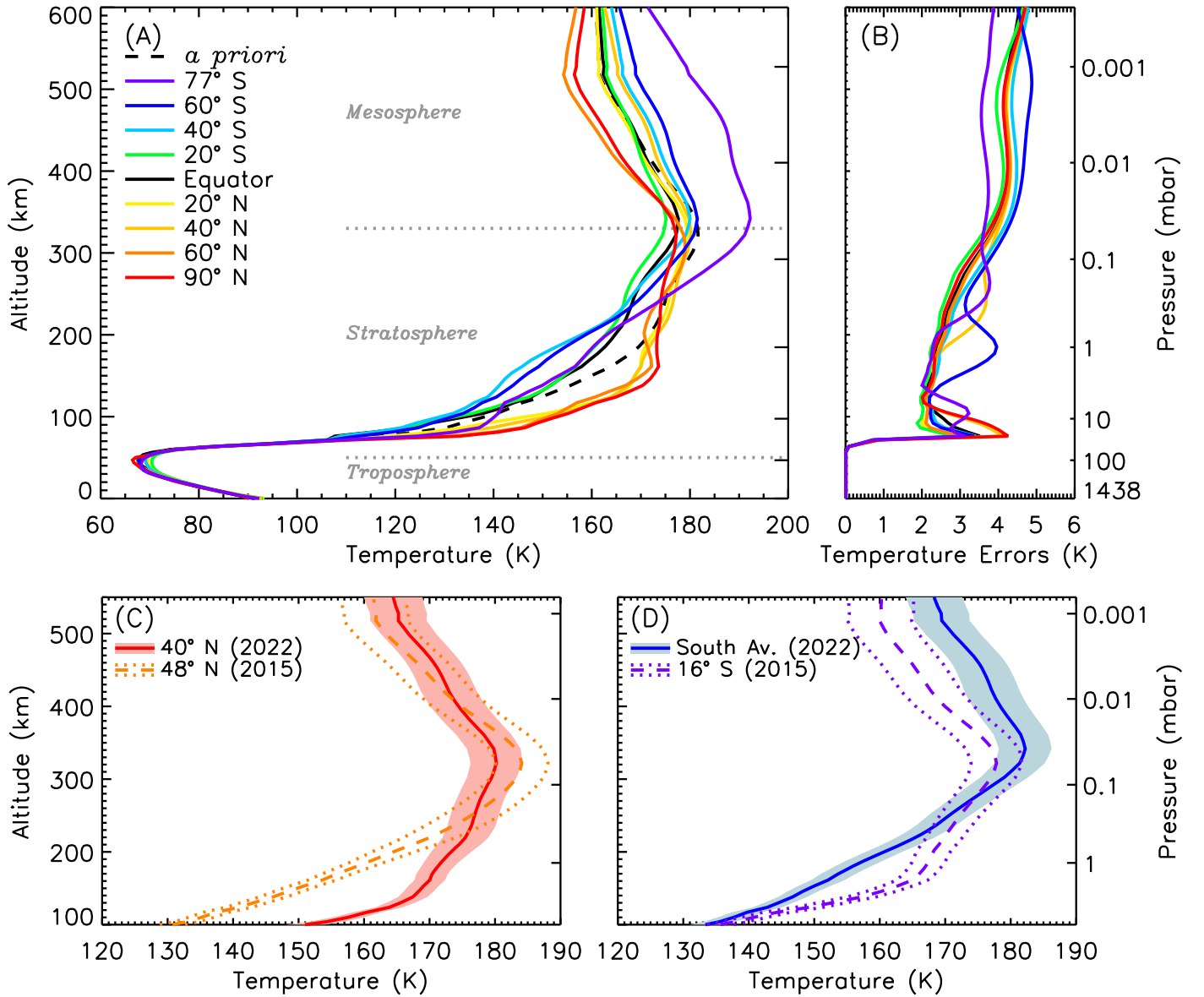
Figure 4. (A) The resulting latitudinally resolved temperature profiles (solid lines) retrieved using the ALMA CO ($J = 6$–5) spectra. The input disk-averaged profile retrieved from previous ALMA observations (Thelen et al. 2020) is shown (dashed black line). (B) The retrieval errors corresponding to the vertical profiles in panel (A). Errors below ∼80 km are tapered to 0 K to hold the tropospheric temperature values to those derived from the Cassini Radio Science data (Schinder et al. 2020). (C) Comparison of the retrieved temperature profile from Thelen et al. (2018) over a range of northern latitudes (centered at ∼48°N; dashed orange profile and dotted errors) and the profile presented here at 40°N (solid red profile and error envelope). (D) Comparison of the retrieved temperature profile from Thelen et al. (2018) representing low southern latitudes (∼16°S; dashed purple profile and dotted errors) and an average of the profiles retrieved here from 20°S to 77°S (solid blue profile and error envelope). The pressure axis on all panels is approximate, represented by the pressures from equatorial latitudes.

A decrease of northern stratopause temperatures was observed during the course of the Cassini mission as Titan's northern hemisphere transitioned out of winter and into spring, accompanied by the elevation of southern stratopause temperatures through the adiabatic heating induced by the subsiding branch of the meridional circulation cell—particularly at the south pole—beginning shortly after Titan's 2009 spring equinox ($L_S = 0°$) (Teanby et al. 2012; Vinatier et al. 2015) and persisting until northern summer solstice ($L_S = 90°$) in 2017 (Teanby et al. 2019; Coustenis et al. 2018, 2020; Vinatier et al. 2020; Mathé et al. 2020; Achterberg 2023). The circulation of Titan's middle atmosphere was predicted by modeling efforts and matched well with Cassini observations (see, for example, Crespin et al. 2008; Lora et al. 2015; Shultis et al. 2022; Lombardo & Lora 2023). For comparison with

these circulation model studies, we show our derived temperature profiles as a function of latitude and altitude in Figure 5. Though the viewing geometry of our observations prohibits the retrieval of temperatures at the south pole, the temperature map shown in Figure 5 is in good agreement with the distribution predicted by circulation models of Titan's northern summer (see Figure 1 in Shultis et al. 2022 or Figure 5 in Lombardo & Lora 2023) and those found through IR measurements toward the end of the Cassini mission (see, e.g., Figure 3 in Teanby et al. 2017; Figure 2 in Vinatier et al. 2020; Figure 6 in Achterberg 2023); indeed, it is also similar to CIRS measurements derived during Titan's northern winter, though now mirrored about the equator (Achterberg et al. 2008, 2011; Vinatier et al. 2015). Previous observations also include a similar stratopause minimum at the low latitudes in the winter
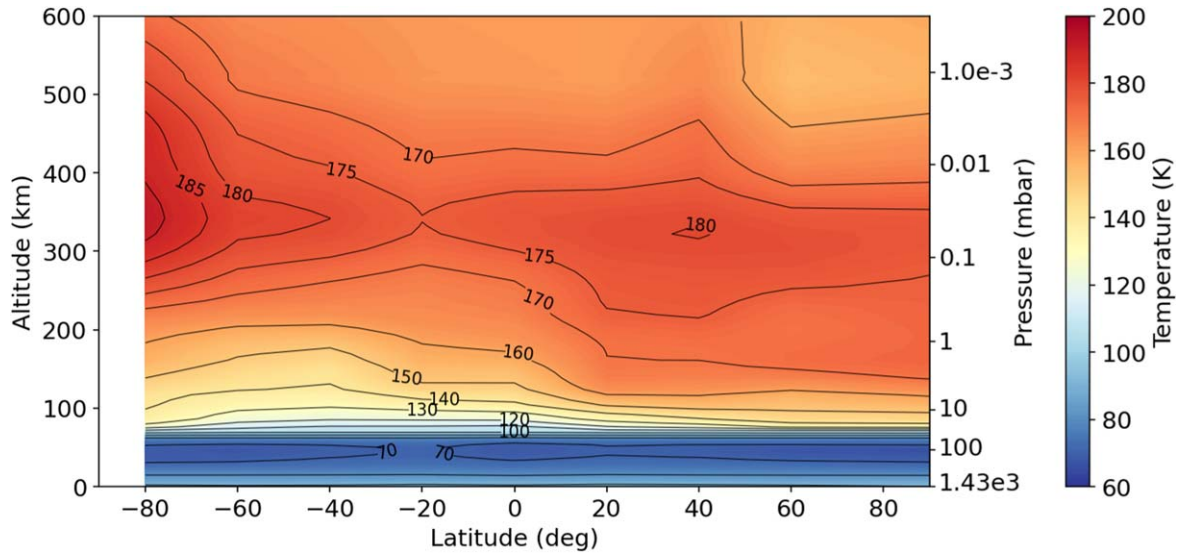
Figure 5. Temperatures from Figure 4(A), shown as a map as a function of latitude and altitude over the vertical range where our ALMA observations are sensitive. The latitudes below 80°S are not shown due to Titan's subobserver latitude at the time of these observations, which shrouds the south pole from view. Temperature contours are shown for reference, as is an approximate pressure grid from equatorial latitudes.

hemisphere (see the saddle point at 20°S in Figure 5). Future ALMA observations of Titan at similar angular resolution will allow for the temporal measurement of the atmospheric temperature structure and assess changes over Titan's northern summer and, in particular, during its autumnal equinox ($L_S = 180°$) in 2025. Here, we may expect the large-scale circulation of the middle atmosphere to break down and eventually reverse, thus completing the seasonal cycle that began with the Cassini observations of Titan in 2004.

4.2. CH$_3$CN Abundances

The retrieved CH$_3$CN profiles are shown in Figure 6(A), and their errors (as a fraction of the CH$_3$CN abundance) are in Figure 6(B). As discussed in Thelen et al. (2019b), ALMA observations of CH$_3$CN are not sensitive to variations in abundance below ∼160 km; this is evidenced by the strong influence of the chosen a priori profile (here, taken from Marten et al. 2002) on the retrieved profiles at low altitudes. The retrieved vertical profiles for CH$_3$CN show a decrease in volume mixing ratio (VMR) with increasing northern latitude, particularly at latitudes north of the equator. The equatorial profile itself is generally in good agreement with the profiles derived by previous (sub)millimeter observations (Marten et al. 2002; Thelen et al. 2019b; Lellouch et al. 2019) and photochemical model predictions above >200 km (Loison et al. 2015; Vuitton et al. 2019). In the stratosphere (∼250 km), the CH$_3$CN abundances at high southern latitudes are enhanced by a factor of ∼5 compared to the north pole. At higher altitudes (>400 km), where the ALMA data become less sensitive, the abundance profiles are largely similar to the equatorial profile south of 40°N. The differences in the vertical profiles match the emission map in Figure 2(B), though with some additional vertical structure at altitudes of <200 km, potentially revealing the influence of Titan's circulation cell on the CH$_3$CN distribution.

As the photochemical lifetime of CH$_3$CN in Titan's middle atmosphere (∼300 km) is predicted to be on the order of 1×10^9–1×10^{11} s (∼32–3200 Earth yr; Wilson & Atreya 2004;

Loison et al. 2015; Vuitton et al. 2019)—and thus significantly longer than Titan's ∼29.5 yr orbital period—the spatial distribution of CH$_3$CN will be driven dynamically rather than by photodissociation and chemistry. The dynamical or transport lifetime of a species is calculated for individual photochemical species based on vertical and molecular diffusion (Loison et al. 2015; Vuitton et al. 2019), which can then be used to predict the species' stratospheric polar enrichment when compared to its photochemical lifetime and Titan's year (Teanby et al. 2009a, 2009b). The observed distribution is further influenced by vertical and horizontal transport from Titan's winds and circulation. Indeed, the photochemical lifetime of CH$_3$CN is longer than its dynamical lifetime by a factor of ∼100, as calculated by the models of Wilson & Atreya (2004), Loison et al. (2015), and Vuitton et al. (2019), and comparable to that of HCN. Thus, it is reasonable to expect CH$_3$CN to be enriched by a factor of <10 at latitudes >60°N by comparison with the enhancements measured by Cassini/CIRS during Titan's northern winter for HCN and other long-lived molecular species, which were found to be distinctly different than the detected short-lived hydrocarbon species (e.g., C$_3$H$_4$, C$_4$H$_2$; Teanby et al. 2008b, 2009b, 2010b). We measure an enhancement factor of ∼1.5 when comparing the profiles retrieved from spectra at ∼77°S (our furthest southern latitude) with those from the equator (see Figure 6(A)). Despite the range of predicted photochemical lifetimes in Titan's stratosphere for CH$_3$CN, our factor is comparable to the predicted enhancement factor of 3 by Teanby et al. (2010b) based on other photochemical species and the photochemical model of Wilson & Atreya (2004). However, without direct measurements of CH$_3$CN at Titan's winter pole—obscured by the viewing geometry here—it is difficult to discern the exact enhancement factor. Our current measurement places CH$_3$CN somewhat in line with the longer-lived (lifetimes >100 yr) hydrocarbon species (e.g., C$_2$H$_6$, C$_3$H$_8$) and CO$_2$ as observed during the Cassini mission, which were all observed to be enhanced by factors of ∼1−5 (Teanby et al. 2008b, 2009a, 2009b, 2010b; Coustenis et al. 2010). This corroborates the predicted dynamical lifetime of CH$_3$CN by
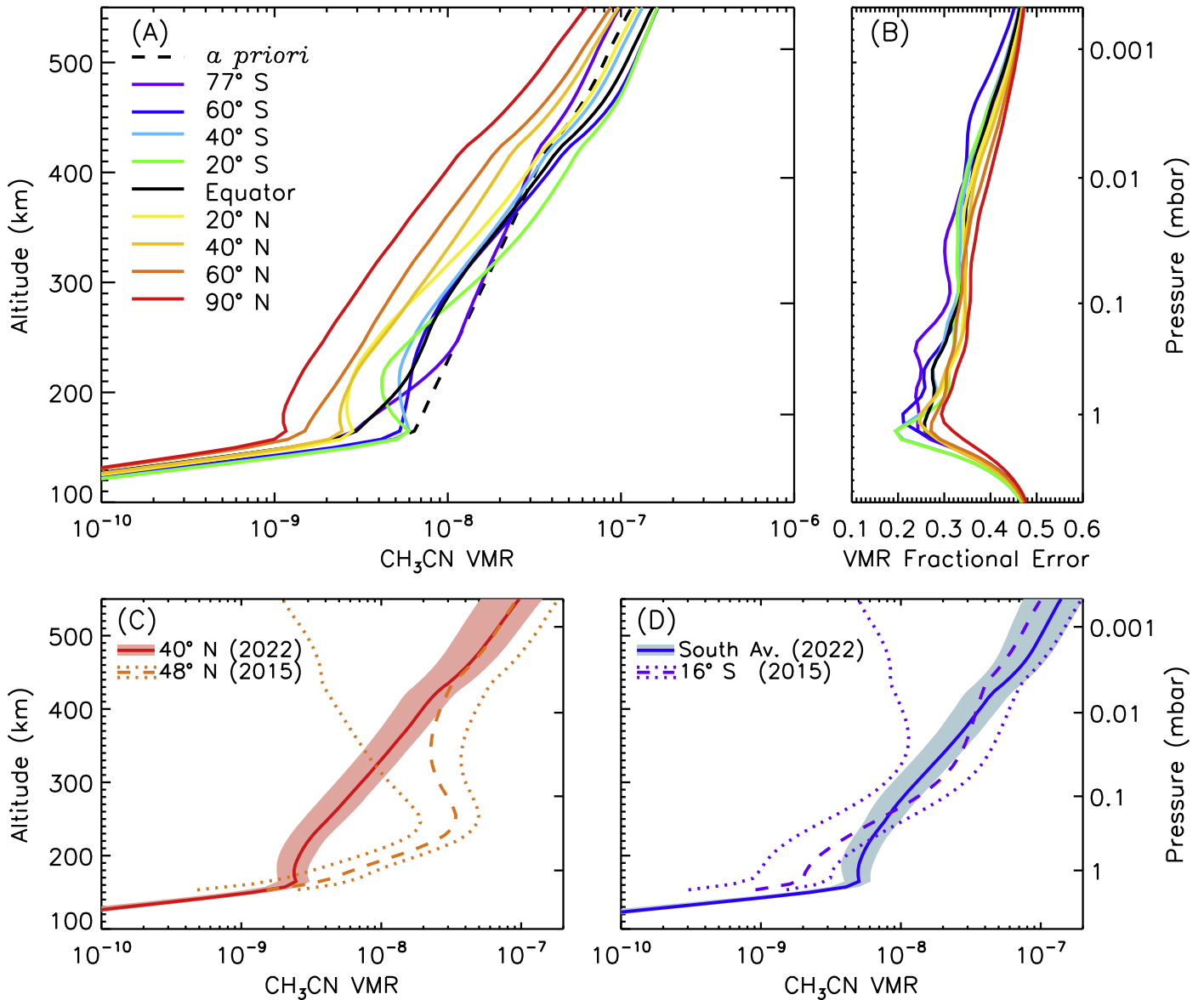
Figure 6. (A) The resulting latitudinally resolved profiles of CH$_3$CN abundance (solid lines) retrieved from ALMA CH$_3$CN ($J = 38–37$) spectra. The retrievals are shown in a similar altitude range as the retrieved temperature profiles (Figure 4), though the CH$_3$CN spectra are not sensitive to abundance variations below ~160 km and above ~450 km. The a priori CH$_3$CN profile, constructed from the observations by Marten et al. (2002) and photochemical model predictions by Loison et al. (2015), is shown (dashed black line). (B) The fractional VMR error profiles corresponding to the vertical profiles in panel (A). (C) Temporal comparison of the CH$_3$CN vertical profile retrieved at 40°N (solid red line and error envelope) to ALMA observations in 2015 (dashed orange profile and dotted errors) from Thelen et al. (2019b). (D) Comparison of an average of southern hemisphere profiles derived here (solid blue line and error envelope) to the vertical profile representing low southern latitudes in 2015 (purple dashed profile and dotted errors) from Thelen et al. (2019b).

Loison et al. (2015) and the transport lifetime by Vuitton et al. (2019), both of which are ~91 yr at 300 km.

As with the temperature profiles, a comparison to previous ALMA retrievals of CH$_3$CN abundance is shown in Figures 6(C) and (D). Here, we see a decrease in northern abundances by a factor of ~16 over roughly a Titan season (7 yr). Despite the stark enhancement in emission over the south pole shown in Figure 2(B), the abundances at high southern latitudes have only increased by a factor of ~1.5−2 over this time period. However, it should be noted again that neither of these ALMA observations were able to retrieve the true vertical profile over the south pole, where the accumulation of CH$_3$CN may be more significant. Additionally, as noted in past works (Thelen et al. 2019b), the relatively large ALMA beam may preclude us from measuring large enhancements with latitude

due to smearing of the emission. Displaying the retrieved abundances as a function of latitude and altitude (Figure 7) shows a shallower CH$_3$CN abundance gradient than species with shorter lifetimes as observed by Cassini/CIRS (e.g., HC$_3$N, C$_2$N$_2$; Teanby et al. 2009a, 2009b), but the increased abundances at altitudes of <200 km between 20°S and 60°S relative to the equator show similarities to maps of the returning circulation branch in the lower stratosphere, manifesting as a "tongue" of enriched air moving equatorward (Teanby et al. 2008a). This was present in the similarly long-lived HCN during Titan's northern winter but surprisingly also in C$_4$H$_2$ (Teanby et al. 2008a). Though the predicted photochemical lifetimes of some species may be incorrect, it is also possible that alternative or additional sources of neutral and ion species production, such as galactic cosmic rays,
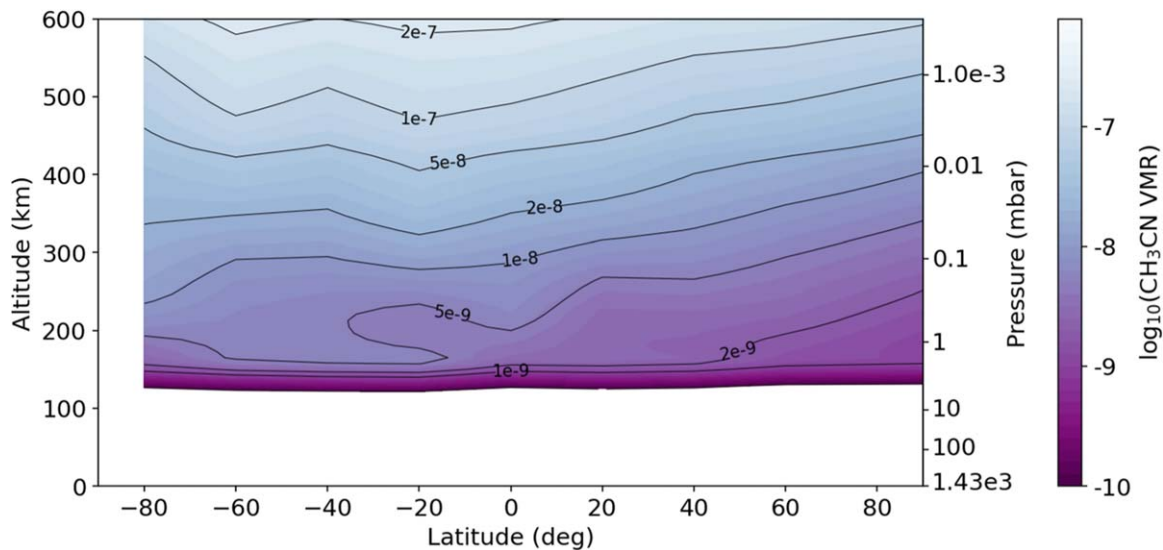
Figure 7. Map of CH₃CN abundances as a function of latitude and altitude. The pressure axis is approximate, represented by the pressures from equatorial latitudes.
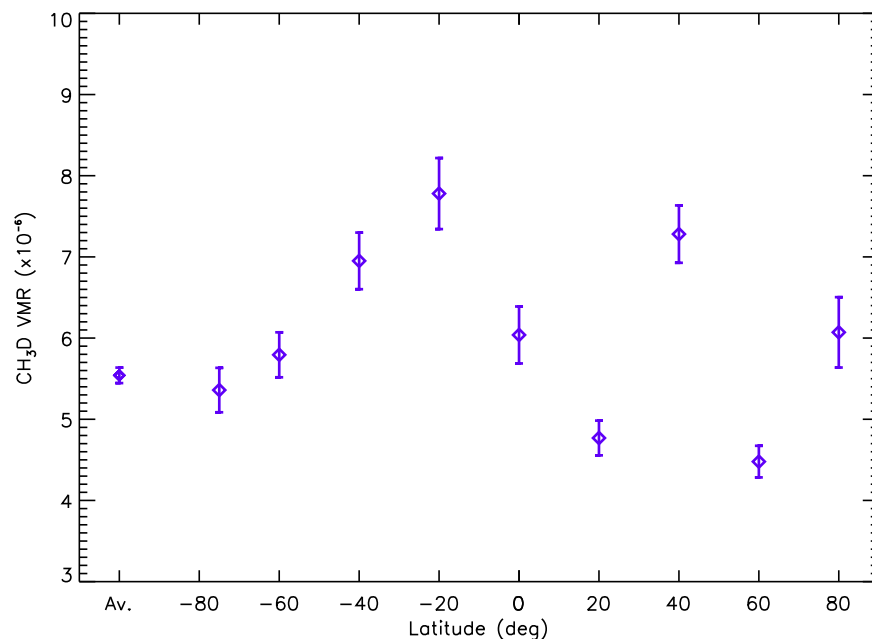

Figure 8. CH₃D abundance in Titan's stratosphere (between ∼100 and 300 km; ∼0.1–10 mbar). The retrieval error bars are shown for each data point. Each data point represents the averaged atmospheric CH₃D VMR for latitudes spanning ∼±10° (low latitudes) to ∼±20° (high latitudes) due to the size of the ALMA beam and the subobserver latitude of Titan (∼12°), as shown in Figure 2(C). The weighted average of all observations is shown (leftmost data point).

increase the stratospheric abundances (Loison et al. 2015). Additional observations of CH₃CN in the future may shed light on the changing distribution of this species and the potential for it to track the returning branch of the meridional circulation cell.

4.3. CH₃D Abundances

The stratospheric CH₃D abundances averaged across both hemispheres are shown in Figure 8. As in the emission map in Figure 2(A), there is significant spread in the retrieved CH₃D abundances. The range of measurements, ∼4−8 ppm, encapsulates the values previously measured by the ISO (Coustenis et al. 2003), ground-based observations (Penteado et al. 2005), and Cassini (Bézard et al. 2007; Coustenis et al. 2007;

Abbas et al. 2010; Nixon et al. 2012; Rannou et al. 2022); the weighted average of all latitudes is $(5.54 \pm 0.10) \times 10^{-6}$ (shown as the leftmost point in Figure 8). When taken with the previously derived D/H ratio based on the Cassini/Huygens CH₄ measurements, the converted CH₄ abundances are found to vary between 0.9% and 1.6%, as shown in Figure 9. We find that the values at ±40°S and 20°S exhibit values around the 1.48% level as measured by the Huygens/GCMS (Niemann et al. 2010). The converted weighted average CH₄ abundance $=1.15\% \pm 0.02\%$ (leftmost point in Figure 9), which agrees with previous Cassini averages of ∼1.1% CH₄ in the stratosphere (Lellouch et al. 2014; Rannou et al. 2021, 2022). These and other disk-averaged observations (e.g., those with the Herschel space telescope; Courtin et al. 2011; Moreno et al. 2012b; Rengel et al. 2014) indicate more
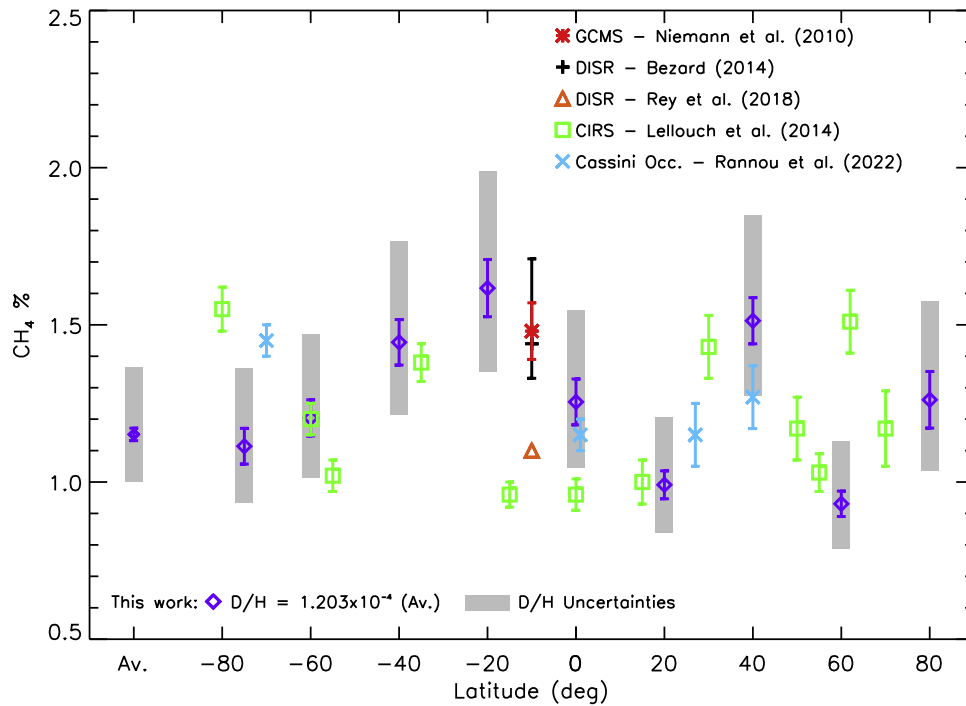
Figure 9. Converted CH_4 abundances as a function of latitude from Figure 8 using the D/H derived in Thelen et al. (2019a) are shown in purple. The weighted average of the converted CH_4 abundance is shown to the left. The shaded error envelopes illustrate the range of converted CH_4 abundances after considering the D/H ratios from ALMA ($=1.033 \times 10^{-4}$; Thelen et al. 2019a) and CIRS ($=1.36 \times 10^{-4}$; Nixon et al. 2012 and references therein). The CH_4 abundances found by the Huygens GCMS (Niemann et al. 2010) and DISR (Bézard 2014; Rey et al. 2018) are shown (red, black, and orange data points, respectively). Green squares show the average measurements of stratospheric CH_4 derived from Cassini/CIRS by Lellouch et al. (2014). Abundances between ~150 and 200 km from Cassini occultation measurements are shown by blue crosses (Rannou et al. 2021, 2022).

variability in Titan's stratospheric methane than was previously expected; many observations now indicate that the stratospheric methane content is lower than the Huygens/GCMS value derived during the probe's descent at ~10°S (Rey et al. 2018).

However, the range of CH_4 values we derive through CH_3D is complicated by the lack of an independent CH_4 profile, and thus the D/H uncertainty must be considered as well. The global average CH_4 value in Figure 9 shows a representative range of the inferred methane abundances when converted using different D/H ratios, which are in the range of ~$(1.0-1.4) \times 10^{-4}$ as derived and discussed in Nixon et al. (2012) and Thelen et al. (2019a). While the atmospheric D/H ratio is not expected to vary with latitude, the range of measured D/H values adds additional uncertainty to the CH_4 abundances inferred through the measurement of CH_3D, increasing our range of converted CH_4 abundances to ~0.8% -1.9% with a global weighted average of $1.15^{+0.21}_{-0.15}\%$.

The comparison of our converted CH_4 abundances to the variability measured by Lellouch et al. (2014) and Rannou et al. (2022) with Cassini IR and occultation measurements is also shown in Figure 9 (green squares and blue crosses, respectively), as are the abundances derived from the Huygens/GCMS and DISR instruments (Niemann et al. 2010; Bézard et al. 2014; Rey et al. 2018). While our averaged and equatorial measurements are lower than those measured by Niemann et al. (2010) and Bézard et al. (2014) with the Huygens probe, they are somewhat consistent with the DISR reanalysis by Rey et al. (2018) following the development of newer spectroscopic CH_4 line data. In some instances, our converted CH_4 abundances are in good agreement with those measured with Cassini/CIRS and through VIMS occultations. At 40°S, 20°S, and 40°N, however,

the CH_4 values are elevated by ~0.4%–0.5% (i.e., 30%–40% greater than the global average value); these locations also correspond to the enhancements on the integrated emission map (Figure 2(A)). Lellouch et al. (2014) note that the mixing timescale of CH_4 in Titan's stratosphere is long enough that enhancements caused by tropospheric injection of methane-enriched air may persist for a large portion of Titan's year; here, we see that this may explain the agreement of values between these works at certain latitudes, as the data analyzed by Lellouch et al. (2014) originate from Cassini observations almost 15 yr prior to these ALMA observations. However, discrepancies where the ALMA-derived abundances are considerably higher (e.g., 20°S, 40°N) exist. These may be the result of more recent injections that have altered the stratospheric CH_4 reservoir following the Cassini measurements, as cloud activity was observed to be more pronounced at midnorthern latitudes in Cassini/VIMS and Imaging Science Subsystem data following Titan's spring equinox (Turtle et al. 2018). Additionally, the equinoctial turnover of Titan's middle atmospheric circulation cell between these observational epochs may be responsible for redistributing locally enhanced methane to southern latitudes; this may explain the difference between the value retrieved here at 20°S and that found by Lellouch et al. (2019). The dearth of CH_4 measured by ALMA in some locations (e.g., 60°N) compared to Cassini may be the result of the previously observed enhancements relaxing to a well-mixed state due to the changes in circulation during this period.

Rannou et al. (2021) postulated that upwelling from more humid tropical regions of the troposphere breaks through the tropopause and injects higher abundances of CH_4 into specific, localized stratospheric latitudes, which they find at 70°S, ~165 km. Comparing the lower stratospheric enhancement

evident in the southern CH$_4$ vertical profile (1.45%, as corrected in Rannou et al. 2022) to equatorial measurements (1.15%), abundances at higher stratospheric altitudes (1.05% at 250 km), and the measurements from Lellouch et al. (2014) at a number of latitudes and altitudes, they propose a complex stratospheric CH$_4$ distribution influenced by both Titan's meridional circulation and upwelling from localized humid regions of the troposphere based on climate modeling predictions (Rannou et al. 2006); see Figure 3 in Rannou et al. (2021). As the Cassini CIRS and VIMS observations were acquired during Titan's northern winter and spring, we may expect both potential new enhancements in the stratosphere from tropospheric injection in the northern latitudes, as well as the redistribution of previously observed enhancements throughout Titan's long seasonal cycle. Here, our measured enhancements at 40°N and 80°N compared to the global average may be the result of upwelling air at humid tropospheric latitudes between ∼30°N and 60°N, which results in additional CH$_4$ distributed to higher northern latitudes and toward the equator. A small secondary circulation cell moving from the midnorthern latitudes poleward has been predicted by circulation models of Titan's atmosphere during the northern summer (see, e.g., Lombardo & Lora 2023). We measure <1% CH$_4$ at 60°N, less than the previous measurement of ∼1.5% in Lellouch et al. (2014), indicating that this may be primarily where the tropospheric upwelling is occurring and bifurcating to poleward and equatorward circulation cells. Indeed, this is where the polar circulation cell of Lombardo & Lora (2023) is observed during northern summer, mirrored from the southern summer circulation cell at ∼50°S–60°S in earlier models (Lora et al. 2015). This is invoked by Rannou et al. (2021) to explain their measured stratospheric methane distribution and the relatively methane-dry value measured by Lellouch et al. (2014) at ∼55°S. Meanwhile, the drop-off in CH$_4$ from the enhancement measured at 20°S to close to the average at 80°S may be the result of the reversed meridional circulation distributing CH$_4$ toward the southern hemisphere.

Of course, these interpretations should be taken with caution, as the distribution of CH$_4$ clearly appears to be complex, evolving, and influenced by both middle and lower atmospheric circulation and climate. Multiple factors contributing to these measurements and interpretations are beyond the capabilities of our ALMA observations, including independent knowledge of the stratospheric methane itself or the means to derive the D/H separately from the reliance on previous measurements as well as the temperature profile of the troposphere, which was taken into account when discussing previous CH$_4$ measurements by Cassini and used to infer the tropospheric methane abundance through saturation vapor pressure for comparison to stratospheric values. Currently, the relatively low-S/N CH$_3$D emission also prohibits the retrieval of a vertical profile, which would provide much more insight into the influence of circulation on the interpretation of these measurements (as it does for the other trace atmospheric species). Local vertical enhancements of CH$_4$ were found at different stratospheric altitudes compared to the background (∼1.1%–1.2%) in the Cassini data analyzed by previous authors (Lellouch et al. 2014; Rannou et al. 2021, 2022), allowing for more complete inferences to be made on the impact of the atmosphere's dynamical state on the CH$_4$ distribution. Our measurements of the CH$_4$ abundance should be taken as averages over a large vertical range (∼100–300

km); as such, the comparison of these values to previous studies at both different times and altitudes complicates an already inconsistent picture. The proposed time-variable influences of circulation, cloud activity, and tropospheric injection remain somewhat speculative until further studies can improve both the D/H certainty and the vertical profile of the CH$_3$D measurements. Still, the aggregate CH$_3$D measurements imply both a distribution of stratospheric methane that is more complex than previously thought (corroborating the studies by Lellouch et al. 2014 and Rannou et al. 2021) and that the global average CH$_4$ abundance in the stratosphere—even when including the known spread of D/H values—is depleted when compared to that of the initial Huygens measurements. This indicates that the single CH$_4$ profile from ∼10°S in 2005 ($L_S \approx 300°$) should be used with caution when considering other latitudes and epochs.

5. Conclusions

We have analyzed interferometric observations of Titan in 2022 ($L_S \approx 146°$) following its northern summer solstice, demonstrating seasonal changes in a heretofore sparsely investigated portion of Titan's year. ALMA Band 9 observations (∼690−710 GHz) enabled the retrieval of abundance and temperature data from multiple latitudinal regions across the disk, which allow us to continue monitoring the atmospheric structure and chemistry after the end of the Cassini mission. Through the analysis of these observations, we find the following:

1. Titan's stratospheric temperature structure in 2022 is similar to that near the northern summer solstice in 2017 and mirrors the distribution of stratospheric temperatures observed during the northern winter at the start of the Cassini mission (2004; $L_S \approx 293°$).

2. For the first time, we retrieve vertical profiles of acetonitrile (CH$_3$CN) abundance that exhibit an enhancement in the southern hemisphere. Abundances are enhanced by factors of ∼1.5–5 compared to the equator and the north pole, but the northern hemisphere abundances have been depleted by up to a factor of 16 since ALMA observations in 2015 (during northern spring).

3. Measurements of stratospheric CH$_3$D sensitive to averaged abundances between ∼100 and 300 km (∼0.1−10 mbar) reveal a complex distribution of monodeuterated methane, which appears at odds with previous measurements in the IR and from the Huygens probe. Using previously derived D/H values, the inferred CH$_4$ content of the stratosphere can be found to vary between ∼0.8% and 1.9%, with a global average of $1.15^{+0.21}_{-0.15}\%$.

4. Together, these temperature and abundance measurements are indicative of the influence of Titan's large meridional circulation, which warms the upper stratosphere of the winter pole (currently, the south pole) and concentrates the long-lived trace atmospheric species inside the polar vortex. The distribution of methane is further impacted by Titan's tropospheric climate, which complicates the interpretation of the CH$_4$ distribution, but is in general agreement with previous models used to explain the stratospheric distribution during northern winter.

Future observations with ALMA will enable the continued measurement of Titan's atmospheric structure and composition, including into higher altitudes than were typically possible using Cassini infrared data for some chemical species (Thelen et al. 2022). Higher-sensitivity (sub)millimeter investigations of Titan's CH_3D may allow for the retrieval of vertical profiles, which will shed additional light on the impacts of tropo- and stratospheric climate and circulation on Titan's stratospheric methane.

ORCID iDs

Alexander E. Thelen ● https://orcid.org/0000-0002-8178-1042
Conor A. Nixon ● https://orcid.org/0000-0001-9540-9121
Martin A. Cordiner ● https://orcid.org/0000-0001-8233-2436
Emmanuel Lellouch ● https://orcid.org/0000-0001-7168-1577
Sandrine Vinatier ● https://orcid.org/0000-0001-5541-2502
Nicholas A. Teanby ● https://orcid.org/0000-0003-3108-5775
Bryan Butler ● https://orcid.org/0000-0002-5344-820X
Steven B. Charnley ● https://orcid.org/0000-0001-6752-5109
Richard G. Cosentino ● https://orcid.org/0000-0003-3047-615X
Katherine de Kleer ● https://orcid.org/0000-0002-9068-3428
Patrick G. J. Irwin ● https://orcid.org/0000-0002-6772-384X
Mark A. Gurwell ● https://orcid.org/0000-0003-0685-3621
Zbigniew Kisiel ● https://orcid.org/0000-0002-2570-3154
Raphael Moreno ● https://orcid.org/0000-0002-9171-2702

References

Abbas, M., Kandadi, H., LeClair, A., et al. 2010, ApJ, 708, 342
Achterberg, R. K. 2023, PSJ, 4, 140
Achterberg, R. K., Conrath, B. J., Gierasch, P. J., Flasar, F. M., & Nixon, C. A. 2008, Icar, 194, 263
Achterberg, R. K., Gierasch, P. J., Conrath, B. J., Flasar, F. M., & Nixon, C. A. 2011, Icar, 211, 686
Bauduin, S., Irwin, P. G. J., Lellouch, E., et al. 2018, Icar, 311, 288
Bézard, B. 2014, Icar, 242, 64
Bézard, B., Marten, A., & Paubert, G. 1992, BAAS, 24, 953
Bézard, B., Marten, A., & Paubert, G. 1993, BAAS, 125, 1100
Bézard, B., Nixon, C. A., Kleiner, I., & Jennings, D. E. 2007, Icar, 191, 397
Bézard, B., Vinatier, S., & Achterberg, R. K. 2018, Icar, 302, 437
Bézard, B., Yelle, R., & Nixon, C. A. 2014, in Titan, ed. I Müller-Wodarg et al. (Cambridge: Cambridge Univ. Press), 158
Borysow, A. 1991, Icar, 92, 273
Borysow, A., & Frommhold, L. 1986a, ApJ, 311, 1043
Borysow, A., & Frommhold, L. 1986b, ApJ, 303, 495
Borysow, A., & Frommhold, L. 1986c, ApJ, 304, 849
Borysow, A., & Frommhold, L. 1987, ApJ, 318, 940
Borysow, A., & Tang, C. 1993, Icar, 105, 175
Braatz, J., Biggs, A., Sanhueza, P., & Corvillon, A. 2021, ALMA Cycle 8 2021 Proposer's Guide, ALMA Doc. 8.2 v1.0, ALMA, https://almascience.eso.org/documents-and-tools/cycle8/alma-proposers-guide
Brogan, C. L., Hunter, T. R., & Fomalont, E. B. 2018, arXiv:1805.05266
Butler, B. J., & Bastian, T. S. 1999, in ASP Conf. Ser. 180, Synthesis Imaging in Radio Astronomy II, A Collection of Lectures from the Sixth NRAO/ NMIMT Synthesis Imaging Summer School, ed. G. B. Taylor, C. L. Carilli, & R. A. Perley (San Francisco, CA: ASP), 625
Camarca, M., de Kleer, K., Butler, B., et al. 2023, PSJ, 4, 142
Cordiner, M. A., Garcia-Berrios, E., Cosentino, R. G., et al. 2020, ApJL, 904, L12
Cordiner, M. A., Palmer, M. Y., Nixon, C. A., et al. 2015, ApJ, 800, L14
Cordiner, M. A., Teanby, N. A., Nixon, C. A., et al. 2019, AJ, 158, 76
Cornwell, T., & Fomalont, E. B. 1999, in ASP Conf. Ser. 180, Synthesis Imaging in Radio Astronomy II, A Collection of Lectures from the Sixth NRAO/NMIMT Synthesis Imaging Summer School, ed. G. B. Taylor, C. L. Carilli, & R. A. Perley (San Francisco, CA: ASP), 187
Cottini, V., Nixon, C. A., Jennings, D. E., et al. 2012, Icar, 220, 855
Courtin, R., Swinyard, B. M., Moreno, R., et al. 2011, A&A, 536, L2
Coustenis, A., Achterberg, R. K., Conrath, B. J., et al. 2007, Icar, 189, 35
Coustenis, A., Jennings, D. E., Achterberg, R. K., et al. 2016, Icar, 270, 409
Coustenis, A., Jennings, D. E., Achterberg, R. K., et al. 2018, ApJL, 854, L30
Coustenis, A., Jennings, D. E., Achterberg, R. K., et al. 2020, Icar, 344, 113413
Coustenis, A., Jennings, D. E., Jolly, A., et al. 2008, Icar, 197, 539
Coustenis, A., Jennings, D. E., Nixon, C. A., et al. 2010, Icar, 207, 461
Coustenis, A., Salama, A., Schulz, B., et al. 2003, Icar, 161, 383
Coustenis, A., Salama, A., Lellouch, E., et al. 1998, A&A, 336, L85
Crespin, A., Lebonnois, S., Vinatier, S., et al. 2008, Icar, 197, 556
Davies, A. G., Sotin, C., Choukroun, M., Matson, D. L., & Johnson, T. V. 2016, Icar, 274, 23
de Bergh, C., Courtin, R., Bézard, B., et al. 2012, P&SS, 61, 85
de Kleer, K., Butler, B., de Pater, I., et al. 2021, PSJ, 2, 5
de Kok, R., Irwin, P. G. J., Teanby, N. A., et al. 2007, Icar, 186, 354
de Pater, I., Sault, R. J., Moeckel, C., et al. 2019, AJ, 158, 139
Dobrijevic, M., Hébrard, E., Loison, J. C., & Hickson, K. M. 2014, Icar, 228, 324
Dudaryonok, A. S., Lavrentieva, N. N., & Buldyreva, J. V. 2015, Icar, 256, 30
Endres, C. P., Schlemmer, S., Schilke, P., Stutzki, J., & Müller, H. S. P. 2016, JMoSp, 327, 95
Flasar, F. M., Kunde, V. G., Abbas, M. M., et al. 2004, SSRv, 115, 169
Flasar, F. M., Samuelson, R. E., & Conrath, B. J. 1981, Natur, 292, 293
Glein, C. R. 2015, Icar, 250, 570
Gordon, I. E., Rothman, L. S., Hill, C., et al. 2017, JSQRT, 203, 3
Gordon, I. E., Rothman, L. S., Hargreaves, R. J., et al. 2022, JQSRT, 277, 107949
Gurwell, M. 2004, ApJ, 616, L7
Gurwell, M., Moreno, R., Moullet, A., & Butler, B. 2011, EPSC-DPS Joint Meeting, 270
Hörst, S. M. 2017, JGRE, 122, 432
Hourdin, F., Talagrand, O., Sadourny, R., et al. 1995, Icar, 117, 358
Irwin, P. G. J., Teanby, N. A., de Kok, R., et al. 2008, JSQRT, 109, 1136
Jaeger, S. 2008, in ASP Conf. Ser. 394, Astronomical Data Analysis Software and Systems, ed. R. W. Argyle, P. S. Bunclark, & J. R. Lewis (San Francisco, CA: ASP), 623
Jennings, D. E., Nixon, C. A., Jolly, A., et al. 2008, ApJL, 681, L109
Jennings, D. E., Romani, P. N., Bjoraker, G. L., et al. 2009, JPCA, 113, 11101
Jolly, A., Cottini, V., Fayt, A., et al. 2015, Icar, 248, 340
Jolly, A., Fayt, A., Benilan, Y., et al. 2010, ApJ, 714, 852
Krasnopolsky, V. A. 2009, Icar, 201, 226
Krasnopolsky, V. A. 2014, Icar, 236, 83
Kunde, V. G., Ade, P. A., Barney, R. D., et al. 1996, Proc. SPIE, 2803, 162
Kunde, V. G., Aikin, A. C., Hanel, R. A., et al. 1981, Natur, 292, 686
Lebonnois, S., Burgalat, J., Rannou, P., & Charnay, B. 2012, Icar, 218, 707
Lebonnois, S., Flasar, F. M., Tokano, T., & Newman, C. E. 2014, in Titan, ed. I. Müller-Wodarg et al. (Cambridge: Cambridge Univ. Press), 122
Lellouch, E., Bézard, B., Flasar, F. M., et al. 2014, Icar, 231, 323
Lellouch, E., Gurwell, M. A., Moreno, R., et al. 2019, NatAs, 3, 614
Light, S., Gurwell, M. A., Thelen, A. E., Lombardo, N., & Nixon, C. A. 2024, PSJ, 5, 98
Loison, J. C., Hébrard, E., Dobrijevic, M., et al. 2015, Icar, 247, 218
Lombardo, N. A., & Lora, J. M. 2023, Icar, 390, 115291
Lora, J. M., Lunine, J. I., & Russell, J. L. 2015, Icar, 250, 516

Lunine, J. I., & Atreya, S. K. 2008, NatGe, 1, 159
Maltagliati, L., Bézard, B., Vinatier, S., et al. 2015, Icar, 248, 1
Marten, A., Hidayat, T., Biraud, Y., & Moreno, R. 2002, Icar, 158, 532
Mathé, C., Vinatier, S., Bézard, B., et al. 2020, Icar, 344, 113547
Miller, K. E., Glein, C. R., & Waite, J. H. J. 2019, ApJ, 871, 59
Mitchell, J. L. 2012, ApJL, 756, L26
Mitchell, J. L., Pierrehumbert, R. T., Frierson, D. M. W., & Caballero, R. 2009, Icar, 203, 250
Moreno, R., Lellouch, E., Lara, L. M., et al. 2012a, Icar, 221, 753
Moreno, R., Lellouch, E., Lara, L. M., et al. 2011, A&A, 536, L12
Moreno, R., Lellouch, E., Hartogh, P., et al. 2012b, AAS/DPS Meeting, 44, 504.04
Moreno, R., Marten, A., & Hidayat, T. 2005, A&A, 437, 319
Müller, H. S. P., Schlöder, F., Stutzki, J., & Winnewisser, G. 2005, JMoSt, 742, 215
Müller, H. S. P., Thorwirth, S., Roth, D. A., & Winnewisser, G. 2001, A&A, 370, L49
Newman, C. E., Lee, C., Lian, Y., Richardson, M. I., & Toigo, A. D. 2011, Icar, 213, 636
Niemann, H. B., Atreya, S. K., Bauer, S. J., et al. 2005, Natur, 438, 779
Niemann, H. B., Atreya, S. K., Demick, J. E., et al. 2010, JGRE, 115, E12006
Nixon, C. A. 2024, ESC, 8, 406
Nixon, C. A., Achterberg, R. K., Vinatier, S., et al. 2008, Icar, 195, 778
Nixon, C. A., Ansty, T. M., Lombardo, N. A., et al. 2019, ApJS, 244, 14
Nixon, C. A., Jennings, D. E., Bézard, B., et al. 2013, ApJ, 776, L14
Nixon, C. A., Lorenz, R. D., Achterberg, R. K., et al. 2018, P&SS, 155, 50
Nixon, C. A., Temelso, B., Vinatier, S., et al. 2012, ApJ, 749, 1
Nixon, C. A., Thelen, A. E., Cordiner, M. A., et al. 2020, AJ, 160, 205
Palmer, M. Y., Cordiner, M. A., Nixon, C. A., et al. 2017, SciA, 3, e1700022
Penteado, P., Griffith, C., Greathouse, T., & de Bergh, C. 2005, ApJ, 629, L53
Press, W., Teukolsky, S., Vetterling, W., & Flannery, B. 1992, Numerical Recipes in FORTRAN. The Art of Scientific Computing (2nd ed.; New York: Cambridge Univ. Press)
Rannou, P., Coutelier, M., Rey, M., & Vinatier, S. 2022, A&A, 666, A140
Rannou, P., Coutelier, M., Rivière, E., et al. 2021, ApJ, 922, 239
Rannou, P., Hourdin, F., McKay, C. P., & Luz, D. 2004, Icar, 170, 443
Rannou, P., Montmessin, F., Hourdin, F., & Lebonnois, S. 2006, Sci, 311, 201
Rengel, M., Sagawa, H., & Hartogh, P. 2011, in Advances in Geosciences, Vol. 25, Planetary Science, ed. K. Satake et al. (Singapore: World Scientific), 173
Rengel, M., Shulyak, D., Hartogh, P., et al. 2022, A&A, 658, A88
Rengel, M., Sagawa, H., Hartogh, P., et al. 2014, A&A, 561, A4
Rey, M., Nikitin, A. V., Bézard, B., et al. 2018, Icar, 303, 114

Richards, A. M. S., Moravec, E., Etoka, S., et al. 2022, arXiv:2207.05591
Rothman, L. S., Gordon, I. E., Babikov, Y., et al. 2013, JSQRT, 130, 4
Rothman, L. S., Jacquemart, D., Barbe, A., et al. 2005, JSQRT, 96, 139
Schinder, P. J., Flasar, F. M., Marouf, E. A., et al. 2020, Icar, 345, 113720
Serigano, J., Nixon, C. A., Cordiner, M. A., et al. 2016, ApJ, 821, L8
Sharkey, J., Teanby, N. A., Sylvestre, M., et al. 2020, Icar, 337, 113441
Sharkey, J., Teanby, N. A., Sylvestre, M., et al. 2021, Icar, 354, 114030
Shultis, J., Waugh, D. W., Toigo, A. D., et al. 2022, PSJ, 3, 73
Sylvestre, M., Teanby, N. A., Vinatier, S., Lebonnois, S., & Irwin, P. G. J. 2018, A&A, 609, A64
Teanby, N. A., Irwin, P. G. J., de Kok, R., et al. 2009a, Icar, 202, 620
Teanby, N. A., Irwin, P. G. J., de Kok, R., & Nixon, C. A. 2009b, RSPTA, 367, 697
Teanby, N. A., Irwin, P. G. J., de Kok, R., & Nixon, C. A. 2010a, ApJ, 724, L84
Teanby, N. A., Irwin, P. G. J., de Kok, R., & Nixon, C. A. 2010b, FaDi, 147, 51
Teanby, N. A., Sylvestre, M., Sharkey, J., et al. 2019, GeoRL, 46, 3079
Teanby, N. A., de Kok, R., Irwin, P. G. J., et al. 2008a, JGRE, 113, E12003
Teanby, N. A., Irwin, P. G. J., de Kok, R., et al. 2008b, Icar, 193, 595
Teanby, N. A., Irwin, P. G. J., Nixon, C. A., et al. 2012, Natur, 491, 732
Teanby, N. A., Bézard, B., Vinatier, S., et al. 2017, NatCo, 8, 1586
Thelen, A. E., Cordiner, M. A., Nixon, C. A., et al. 2020, ApJL, 903, L22
Thelen, A. E., de Kleer, K., Camarca, M., et al. 2024, PSJ, 5, 56
Thelen, A. E., Nixon, C. A., Cosentino, R. G., et al. 2022, PSJ, 3, 146
Thelen, A. E., Nixon, C. A., Cordiner, M. A., et al. 2019a, AJ, 157, 219
Thelen, A. E., Nixon, C. A., Chanover, N. J., et al. 2018, Icar, 307, 380
Thelen, A. E., Nixon, C. A., Chanover, N. J., et al. 2019b, Icar, 319, 417
Tobie, G., Lunine, J. I., & Sotin, C. 2006, Natur, 440, 61
Tomasko, M. G., Bézard, B., Doose, L., et al. 2008, P&SS, 56, 648
Turtle, E. P., Perry, J. E., Barbara, J. M., et al. 2018, GeoRL, 45, 5320
Vinatier, S., Bézard, B., & Nixon, C. A. 2007, Icar, 191, 712
Vinatier, S., Bézard, B., Fouchet, T., et al. 2007, Icar, 188, 120
Vinatier, S., Bézard, B., Lebonnois, S., et al. 2015, Icar, 250, 95
Vinatier, S., Bézard, B., Nixon, C. A., et al. 2010, Icar, 205, 559
Vinatier, S., Mathé, C., Bézard, B., et al. 2020, A&A, 641, A116
Vuitton, V., Yelle, R. V., Klippenstein, S. J., Hörst, S. M., & Lavvas, P. 2019, Icar, 324, 120
Willacy, K., Allen, M., & Yung, Y. 2016, ApJ, 829, 79
Wilson, E. H., & Atreya, S. K. 2004, JGRE, 109, E06002
Yelle, R. V. 1991, ApJ, 383, 380
Yung, Y. L., Allen, M., & Pinto, J. P. 1984, ApJS, 55, 465